CrystEngComm

ROYAL SOCIETY OF CHEMISTRY

PAPER

View Article Online
View Journal | View Issue



Cite this: *CrystEngComm*, 2025, **27**, 311

# A novel bis-(triazolyl)-furoxan energetic compound—graphene-like crystal structure for balancing energy and sensitivity†

Jiapeng Wang,[a] Jianhua Wang,[a] Yucun Liu,*[a] Junming Yuan,[a] Yanwu Yu,[a] Yankang Zhang[b] and Xuejian Yan[c]

A novel bis-(1,2,4-triazolyl)-furoxan structure for balancing energy and sensitivity has been successfully achieved. Theoretical calculations and impact sensitivity tests show that bis-(2-methy-3-nitroamine-1,2,4-triazolyl)-furoxan and bis-(2-methy-3-amine-1,2,4-triazolyl)-furoxan of two energetic compounds exhibit outstanding denotation performance (8.1 km $s^{-1}$) and excellent impact sensitivity properties (>25 J). It is demonstrated that the graphene-like layered stacking structure of novel bis-(1,2,4-triazole)-furoxan compounds is due to intramolecular interactions and intermolecular interactions by combining structure description with wavefunction analysis (Hirshfeld surface analysis, IRI analysis, IGMH analysis, AIM analysis, *etc.*). Numerous experiments have shown that 3-nitro-5-chloroxime-1,2,4-triazole or 3-nitroamino-5-chloroxime-1,2,4-triazole of two intermediate compounds is unable to obtain bis-triazole-furoxan under alkaline conditions. *N*-methylation of the triazole was accomplished by protecting the amino group with dimethylformamide dimethylacetal, facilitating furoxan synthesis. This study first introduces the electrostatic potential isosurface distribution of clusters within crystals in analysing energetic compounds. The results show that the electrostatic potential distribution of clusters is more regular than individual molecules, which could be significant for predicting and assessing the sensitivity of energetic compounds.

Received 2nd November 2024,
Accepted 29th November 2024

DOI: 10.1039/d4ce01116c

rsc.li/crystengcomm



## Introduction

The balance between sensitivity and detonation performance has always been a popular area of research for energetic compounds. These compounds tend to have opposite trends of sensitivity and detonation performance. However, there is no conclusive evidence that the low sensitivity and their high detonation performance cannot coexist in a paradoxical relationship. In recent years, furoxan[1] has had a structural building block by linking aromatic compounds such as tetrazoles,[2,3] oxadiazoles,[4,5] oxatriazoles,[6] and benzenes[7,8] to energetic sites or by self-forming dimers[9] and trimers[10,11] through coupling, resulting in a wide variety of energetic compounds, which has made significant progress in the development and research of energetic compounds.[12,13] Studies have shown that furoxan has a distinct advantage due to its unique structure concerning other 5-membered heterocycles.[14] The furoxan ring can form a latent nitroxide inner ring structure with two reactive oxygen atoms, increasing the target compound's oxygen content, enthalpy, and crystal density, which results in a higher detonation performance. 1,2,4-Triazole energetic compounds are more advantageous in balancing the sensitivity and detonation performance due to their excellent backbone structure (high enthalpy of formation, aromaticity, uniform carbon and nitrogen distribution, structural symmetry, *etc.*) compared with the 5-membered rings of oxadiazoles (furazan, furoxan) and unstable nitrogen-linked compounds (1,2,3-triazoles, tetrazoles). Some energetic compounds based on 1,2,4-triazole are well-known for their superb energy and usefulness. Examples include 3-nitro-5-keto-(1,2,4)-triazole (NTO), 3,5-dinitro-1-methyl-1,2,4-triazole (MDNT), and 3-amino-5-nitro-1,2,4-triazole (ANT).

In recent research, the combination of 1,2,4-triazole with furoxan as a bicyclic energetic compound has gained the attention of researchers.[15–17] However, previous studies have only focused on binding a single triazole to the furoxan molecule.[18] Furoxan has two carbon modification sites, which connect the triazole molecules on both sides and can lead to the development of a novel tricyclic energetic compound.[19,20] The structure of bis-(1,2,4-triazolyl)-furoxan is identical to that of bis-(tetrazole)-furoxan previously published.[21] However, the

[a] *School of Environmental and Safety Engineering, North University of China, Taiyuan, 030051, China. E-mail: lyc2ct@vip.Sina.com*
[b] *China Safety Technology Research Academy of Ordnance Industry, Beijing 100053, China*
[c] *Jiangnan Industries Group Co., Ltd., Xiangtan, 411207, China*

† Electronic supplementary information (ESI) available: CCDC 2358185–2358187. For ESI and crystallographic data in CIF or other electronic format see DOI: https://doi.org/10.1039/d4ce01116c

tetrazole's N–N-linked structure is unstable, much like azide compounds. Replacing bis(tetrazole) with bis(1,2,4-triazole) can enhance the safe properties of the furoxan compound. This enhancement increases its energy and decreases sensitivity by modifying the C-site and N-site groups of the triazole. Only one report has been published on the similar structure of bis-(1,2,4-triazolyl)-furoxan from 2012 until now.[22] However, this structure could be enhanced at a molecular level. Introducing a nitro group into triazole at the *N* position can increase energy, but it also makes it impossible to increase energy further, as shown in Fig. 1. Therefore, it is necessary to continue exploring synthetic methods, detonation, and crystal properties of bis-(1,2,4-triazolyl)-furoxan-like energetic compounds. This work delves into the synthesis methods of three novel tricyclic structures of bis-(1,2,4-triazolyl)-furoxan energetic compounds **13**, **14**, and **15**. A combination of crystal analysis and wavefunction analysis investigates the advantages of the bis-(triazole)-furoxan properties for analysing their molecule structural features and crystal stacking.

## Experimental section

### Materials and measurements

All the chemicals and solvents were purchased from Sigma-Aldrich and used without further purification. Compound **1** can be synthesised through three steps, as reported.[23] Compounds **3** and **8** can be synthesised from compound **2** and compound **7**, as reported.[24] Compounds **4**, **6** and **9** cannot be obtained through numerous experiments, as shown in Fig. 2. For spectroscopic characterisation, a small quantity of the solid compound was dissolved in DMSO-$d_6$, and NMR data were acquired on a Bruker AVANCE (400 MHz for $^1$H and 600 MHz for $^{13}$C) spectrometer. FTIR spectra were measured using an FTIR PerkinElmer Frontier spectrometer. The thermal decomposition data were obtained from a PerkinElmer DSC 4000. Compounds **12**, **13**, and **15** were structurally characterised by single-crystal X-ray diffraction at an ambient temperature of 298 K using a Bruker D8 VENTURE single-crystal diffractometer with a graphite monochromator controlled using APEX2. The structures were solved using direct methods using the Shelxtl software. An Elementar Vario is used for elemental analysis (EA).

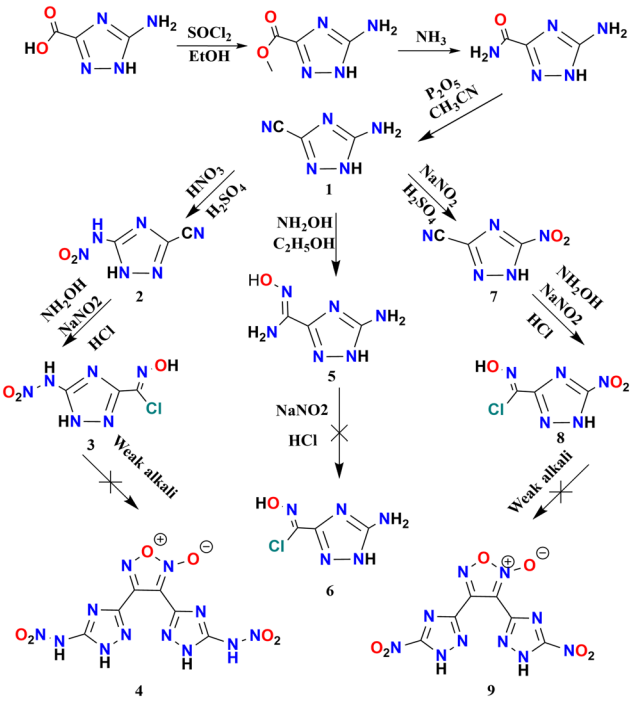


Fig. 2 Failed synthetic routes of compounds **4**, **6** and **9**.

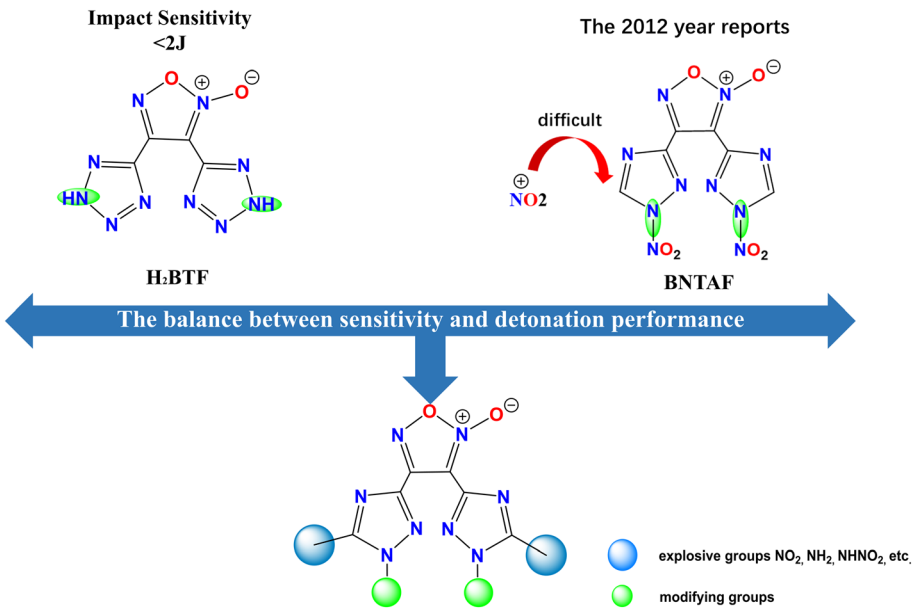


Fig. 1 The structure of bis-(1,2,4-triazolyl)-furoxan of energetic compounds.

 

**Calculation methods.** The prediction for the density of the compounds (**13–15**) was carried out using Peter Politzer's method.[25] The enthalpy of the compounds (**13–15**) was calculated using the PBE0-D3(BJ)/6-311G(**)//PBE0-D3(BJ)/6-31G(**) level *via* Gaussian16; the detonation parameters were predicted *via* the K–J equation;[26] the Hirshfeld surface analysis and the energy framework analysis were carried out *via* the CrystalExplorer software;[27] AIM (Bader's theory of 'atoms in molecules) analysis,[28] electrostatic analysis,[29–31] IRI analysis[32] and IGMH analysis[33] were performed by combining the Multiwfn[34] and the VMD software; the wavefunction files about the electrostatic potential isosurface, IRI and IGMH were obtained through the B3LYP-D3(BJ)/6-311G(**) level calculation. The wavefunction files from the AIM analysis were obtained through the B3LYP-D3(BJ)/ma-TZVPP//B3LYP-D3(BJ)/TZVP level calculation.

**Synthesis of compound 1.** a) Take 3.2 g (22.8 mmol) of 3-formyl-5-amine-1,2,4-triazole and dissolve it in 50 ml of ethanol. Keep the temperature at 0 °C and slowly add 5 ml of thionyl chloride ($SOCl_2$). After heating the reaction mixture under reflux to 90 °C for 2 hours, cool the reaction down to room temperature. Neutralise to neutral with sodium carbonate ($Na_2CO_3$). Filter and collect the white products (3.2 g, 20.5 mmol). Yield 90%. Elemental anal. calcd. (%) for C 38.46, H 5.12, N 35.89, O 20.51; found: C 38.86, H 5.25, N 34.80, O 20.57. IR (KBr, $cm^{-1}$): 3449, 3139, 1723, 1635, 1456, 1240, 1118, 1018, 712.

b) Dissolve 1 g (6.4 mmol) of the product from step a) in 10 ml of 25% ammonia and heat the mixture to 70 °C under closed conditions for 2 hours. Then, cool the reaction down to room temperature. Add acetic acid to the mixture to acidify it until the pH reaches 4. Collect the resulting precipitate by filtration to obtain a white product known as 5-amino-1*H*-1,2,4-triazole-3-carboxamide (0.6 g 4.7 mmol). Yield 72%. Elemental anal. calcd. (%) for C 27.90, H 3.87, N 54.26, O 13.95; found: C 28.34, H 3.94, N 54.90, O 11.70. IR (KBr, $cm^{-1}$): 3340, 3142, 1691, 1646, 1580, 1483, 1415, 1297, 1121, 1069, 763, 687.

c) Add 3 g (23.2 mmol) of product from step b) and 20 g of $P_2O_5$ into 300 ml of anhydrous acetonitrile simultaneously. Stir the mixture for 72 hours at room temperature. Then, 100 ml of distilled water was added to the reaction vessel. Evaporate the acetonitrile in a vacuum and extract the resulting clear solution with ethyl acetate (3 × 100 mL). Dry the combined organic layers over magnesium sulfate. Finally, remove the solvent in a vacuum to obtain a colourless powder (2 g, 18.0 mmol). Yield 77%. Elemental anal. calcd. (%) for C 32.43, H 4.50, N 63.06, O 0; found: C 31.76, H 2.87, N 59.76, O 5.74. IR (KBr, $cm^{-1}$): 3431, 3289, 3147, 2259, 1635, 1557, 1490, 1356, 1120, 1010, 728, 675.

**Synthesis of compound 11.** 0.6 g (5.4 mmol) of compound **1** and 1.2 g of dimethylformamide dimethyl acetal were added simultaneously to 18 ml of acetonitrile. The temperature was gradually raised to 40 °C for 1 hour. The resulting solution was bright orange. The solution was then poured into a tray, and the solvent was left to air-dry naturally to obtain a sample of needle-shaped crystals. Then, 1 g of needle-shaped crystals was added to 2 ml of distilled water. Then, 5 ml of 50% hydroxylamine solution was slowly poured into the mixture, and the reaction was kept for 30 minutes. After adding 15 ml of hydrochloric acid and 3 g of sodium nitrite to the mix, the temperature was maintained at 0 °C. Finally, the yellow powder was filtered (0.6 g, 3.0 mmol). Yield 56%. IR (KBr, $cm^{-1}$): 1597, 1537, 1466, 1394, 1116, 1075, 1013, 942, 887, 825, 727. Elemental anal. calcd. (%) for C 42.63, H 5.58, N 42.63, O 9.13; found: C 42.51, H 5.57, N 42.52, O 9.51. $^1$H NMR (400 MHz, DMSO) $\delta$ 12.97 (s, 1H), 8.62 (s, 1H), 3.70 (s, 3H), 3.19 (s, 3H), 3.09 (s, 3H). $^{13}$C NMR (101 MHz, DMSO) $\delta$ 159.13, 156.56, 148.32, 127.15, 35.16, 34.45, 34.37.

**Synthesis of compound 12.** 1 g (5 mmol) of compound **11** was dissolved in 100 ml tetrahydrofuran. Then, 0.3 grams of sodium carbonate ($Na_2CO_3$) was added directly to the reaction system, and the reaction was carried out at 25 °C for 24 hours. The solution changed from cloudy to clear. Afterwards, the impurities were filtered out, leaving the solution with the dissolved products behind. The colourless product slowly precipitated and was collected (1 g 2.6 mmol). Yield 53%. IR (KBr, $cm^{-1}$): 1620, 1527, 1468, 1392, 1337, 1294, 1109, 1063, 1029, 959, 798. Elemental anal. calcd. (%) for C 44.90, H 5.34, N 44.91, O 4.81; found: C44.54, H 5.69, N 43.37, O 4.02. $^1$H NMR (400 MHz, DMSO) $\delta$ 8.39 (s, 1H), 8.35 (s, 1H), 3.66 (d, $J$ = 16.7 Hz, 6H), 3.11 (d, $J$ = 5.5 Hz, 6H), 3.02 (s, 6H). $^{13}$C NMR (101 MHz, DMSO) $\delta$ 159.32, 157.57, 150.25, 146.83, 143.64, 34.21, 24.98.

**Synthesis of compound 13.** 0.7 g (1.8 mmol) of compound **12** was dissolved in 50 ml of 11% hydrochloric acid solution and reacted 48 hours at 25 °C. The white product slowly precipitated and was collected (0.4 g 1.5 mmol).

Yield 84%. IR (KBr, $cm^{-1}$): 3413, 3322, 3187, 1650, 1574, 1499, 1432, 1293, 1260, 1221, 1075, 964, 837, 767, 667. Elemental anal. calcd. (%) for C 36.36, H 3.70 N 53.03, O 6.81; found: C 37.29, H 3.54, N 54.36, O 6.16. $^1$H NMR (400 MHz, DMSO) $\delta$ 6.53 (d, $J$ = 5.7 Hz, 4H), 3.57 (d, $J$ = 3.8 Hz, 6H). $^{13}$C NMR (101 MHz, DMSO) $\delta$ 156.21, 150.16, 146.47, 143.24, 108.82, 33.58.

**Synthesis of compound 14.** At a temperature of −5 °C, 0.2 g (0.7 mmol) of compound **13** was added to 3 ml of 30% hydrogen peroxide, and then 1.5 ml of concentrated sulfuric acid was slowly added. The temperature was kept below 0 °C. After the addition, the temperature was raised to room temperature. Then 0.5 g of sodium tungstate was added in batches, and the feeding temperature was maintained at room temperature for 4 hours after each batch addition. Finally, the mixture was extracted with ethyl acetate (0.1 g 0.3 mmol). Yield 44%. IR (KBr, $cm^{-1}$): 3087, 2926, 1610, 1509, 1398, 1360, 1282, 1247, 1072, 1043, 964, 896, 822, 747, 709. Elemental anal. calcd. (%) for C 36.36, H 1.85, N 43.20, O 24.69; found: C 36.25, H 2.13, N 43.11, O 24.22. $^1$H NMR (400 MHz, DMSO) $\delta$ 3.58 (d, $J$ = 3.3 Hz, 6H). $^{13}$C NMR (101 MHz, DMSO) $\delta$ 154.85, 148.32, 144.49, 141.34, 107.91, 34.23.

**Synthesis of compound 15.** 0.2 g (0.7 mmol) of compound **13** was added gradually to 10 ml of 98% concentrated sulfuric

acid. Subsequently, 1 ml of fuming nitric acid was slowly added to the reaction mixture, which was carried out at 0 °C for one hour. The yellow-coloured reaction solution was poured into ice water, separating a white product. The product was collected through filtration, and a yield of 0.24 grams was obtained. (0.24 g 6.8 mmol). Yield 97%. IR (KBr, $cm^{-1}$): 3446, 3075, 1805, 1617, 1551, 1500, 1458, 1413, 1379, 1309, 1237, 1144, 1043, 972, 935, 801, 719. Elemental anal. calcd. (%) for C 27.27, H 1.85, N 43.20, O 24.69; found: C 27.00, H 1.70, N 42.12, O 25.51. $^1$H NMR (400 MHz, DMSO) $\delta$ 7.54 (d, 2H), 3.85 (s, 3H), 3.81 (s, 3H). $^{13}$C NMR (101 MHz, DMSO) $\delta$ 148.93, 145.98, 143.64, 138.74, 106.05, 35.35, 35.29.

## Results and discussion

Initially, a synthetic route resulted in the formation of two furoxan energetic compounds **9** and **10** *via* a conventional 1,3-dipolar cycloaddition reaction[35] between nitrile oxides of compound **3** (3-nitroamine-5-chloroxime-(1,2,4-triazole)) and compound **8** (3-nitro-5-chloroxime-(1,2,4-triazole)) under weak-base conditions. Unfortunately, numerous experiments have shown that this synthesis route of compounds **9** and **10** is impossible, as shown in Fig. 2. Different weak bases, such as $K_2CO_3$, $Na_2CO_3$, $Ag_2CO_3$, $MnCO_3$, $CuCO_3$, $ZnCO_3$, $(NH_4)_2CO_3$, pyridine, *etc.*, were tested with various solvents, which include tetrahydrofuran, ethyl acetate, butyl acetate, dioxane, toluene, ether and many ratios of the mixture. The failure can be attributed to three main aspects. In the first aspect, weak bases such as $ZnCO_3$, $(NH_4)_2CO_3$, $MnCO_3$ and pyridine have difficulty reacting with compounds **3** and **8**. In the second aspect, too many impurities are difficult to separate and purify. Our tests have demonstrated that one equivalent of $Na_2CO_3$, $K_2CO_3$, and $Ag_2CO_3$ can help two types of chloroxime (compounds **3** and **8**) react using tetrahydrofuran or ethyl acetate as solvents. The products still contain excessive impurities that are difficult to separate. The third aspect is that compounds **3** and **8** form a residue that is difficult to dissolve when excessive weak bases are used. Only methanol and ethanol may separate organic compounds. However, the furoxan of products is not detected upon solvent evaporation. When the products generated by using $Ag_2CO_3$ conditions are added to excess $NH_3OH$–HCl, $NH_4Cl$, NaCl, KCl, and $BaCl_2$ through substitution reaction, it is not possible to obtain more stable furoxan products in solvents such as methanol, ethanol, acetone, and tetrahydrofuran. Additionally, forming furoxan was abandoned through compound **6** (3-amino-5-chloroxime-(1,2,4-triazole)) because the direct conversion of compound **5** to compound **6** was impossible, as shown in Fig. 2.

It has been concluded that the synthetic route mentioned cannot be achieved due to the nitramine and nitro groups on the 1,2,4-triazole. These groups may cause the entire chloroxime triazole to become highly acidic, making it impossible for the intermediate nitrile oxides to undergo a single 1.3-dipole cycloaddition reaction under weak alkaline conditions. This leads to the production of unwanted by-products. Alternatively, the route can be modified to synthesise the furoxan first and then convert the amine to nitramine and nitro groups. Therefore, protecting the amino group on compound **1** is essential before synthesising the bis-(1,2,4-triazolyl)-furoxan.

As depicted in Fig. 3, the amino group of compound **3** was protected according to the method reported in the literature.[36] However, it was discovered that the nitrogen atom of the triazole containing active hydrogens can act as a nucleophile and attack the carbon atoms of dimethylformamide dimethylacetal. It is demonstrated that the product was not unique when analysed using TLC chromatography. The amino group of the triazole can form a Schiff base, while the imine nitrogen atom on the triazole is protected. It was previously believed that compound **1** could be converted to compound **10** by converting the cyane to chloroxime in a two-step process. It was discovered that methylation of the N atom of the triazole led to the conversion of compound **1** to compound **11**, which was surprising. Unfortunately, compound **10** cannot be obtained. The mechanical reason for the methylation of nitrogen atoms on triazoles remains unclear. The result of *N*-methylation removes the active hydrogen and reduces the acidity of compound **11**. This is likely the primary reason that compound **11** precipitates in acidic solutions without extraction in contrast to compounds **3** and **8**.

Compound **11** was successfully converted to compound **12** (furoxan) with $Na_2CO_3$ in tetrahydrofuran. Under 11% dilute hydrochloric acid conditions, the Schiff base of compound **12** was hydrolysed to produce compound **13**, as shown in Fig. 3. The synthesis of the structural framework of the bis-(1,2,4-triazole)-furoxan energetic compound was completed. The nitro group was introduced *via* nitration and oxidation, forming two higher energetic compounds: compounds **14** and **15**, as depicted in Fig. 4. The single-crystal structures of compounds **12**, **13** and **15** are shown in Fig. 5, and crystal parameters and CCDC numbers are provided in Table S1.†

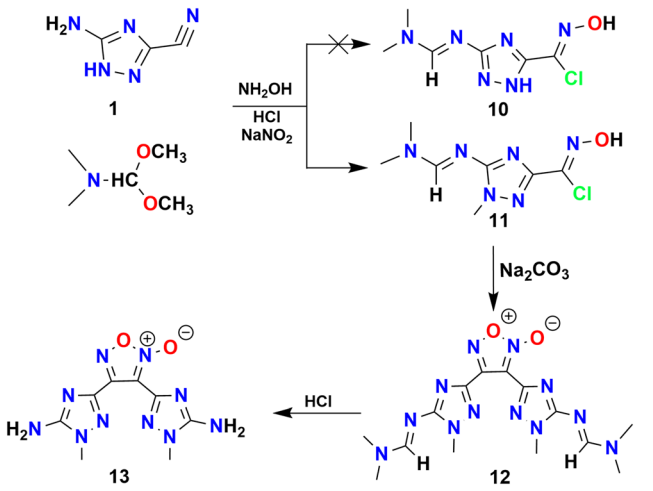


Fig. 3 The synthetic route of compound **13**.

 

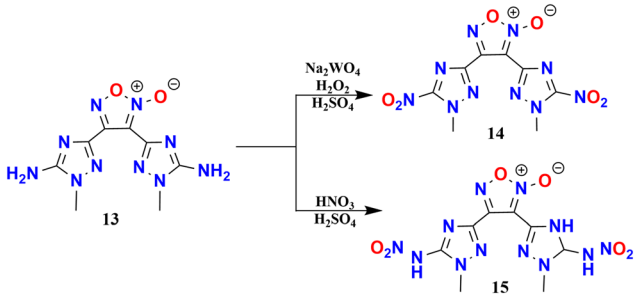


Fig. 4 The synthetic route of compounds **14** and **15**.

The H NMR spectra, C NMR spectra, IR spectra, and DSC thermal analysis diagram for compounds **13–15** are available in Fig. S1–S21 in the ESI.†

### The physical and chemical properties of the compounds (13–15)

The table indicates that the density of compound **13** is 1.68 g $cm^{-3}$, slightly higher than that of $H_2BTF$, which has a density of 1.62 g $cm^{-3}$. However, the explosive performance of compound **13** is significantly lower than that of $H_2BTF$. This discrepancy is mainly attributed to the higher nitrogen content in $H_2BTF$. On the other hand, compound **13** demonstrates a sensitivity exceeding 30 J, indicating a much greater impact energy than $H_2BTF$, which has an impact energy of less than 2 J in terms of sensitivity. The presence of tetrazolyl in $H_2BTF$ enhances its explosive properties due to the N–N linked group. Replacing tetrazolyl with triazolyl in furoxan could significantly improve safety and detonation performance.

The detonation performance of compounds **14** and **15** is slightly lower than that of BNTAF. This difference is attributed to the lower density and enthalpy of formation in compounds **14** and **15** compared to BNTAF. However, their impact sensitivity is much higher than that of BNTAF. Although the impact energy for BNTAF has not been reported, it is noted that the impact sensitivity for BNTAF has an $H_{50}$ of 7.2 cm according to the report in the GJB772A-1997-601-2 method. In contrast, the $H_{50}$ for LLM-105 under 2 kg drop hammer conditions exceeds 100 cm. The impact sensitivity of compound **15** is comparable to that of LLM-105, which exceeds 25 J, indicating that compound **15** has significantly better impact sensitivity than BNTAF. The trade-off of sacrificing some detonation energy is justified to significantly reduce sensitivity in compound **15**. Unfortunately, compound **15** exhibits weak thermal stability, with decomposition occurring at around 144 °C as opposed to the decomposition temperature of compound **13** at 278 °C,

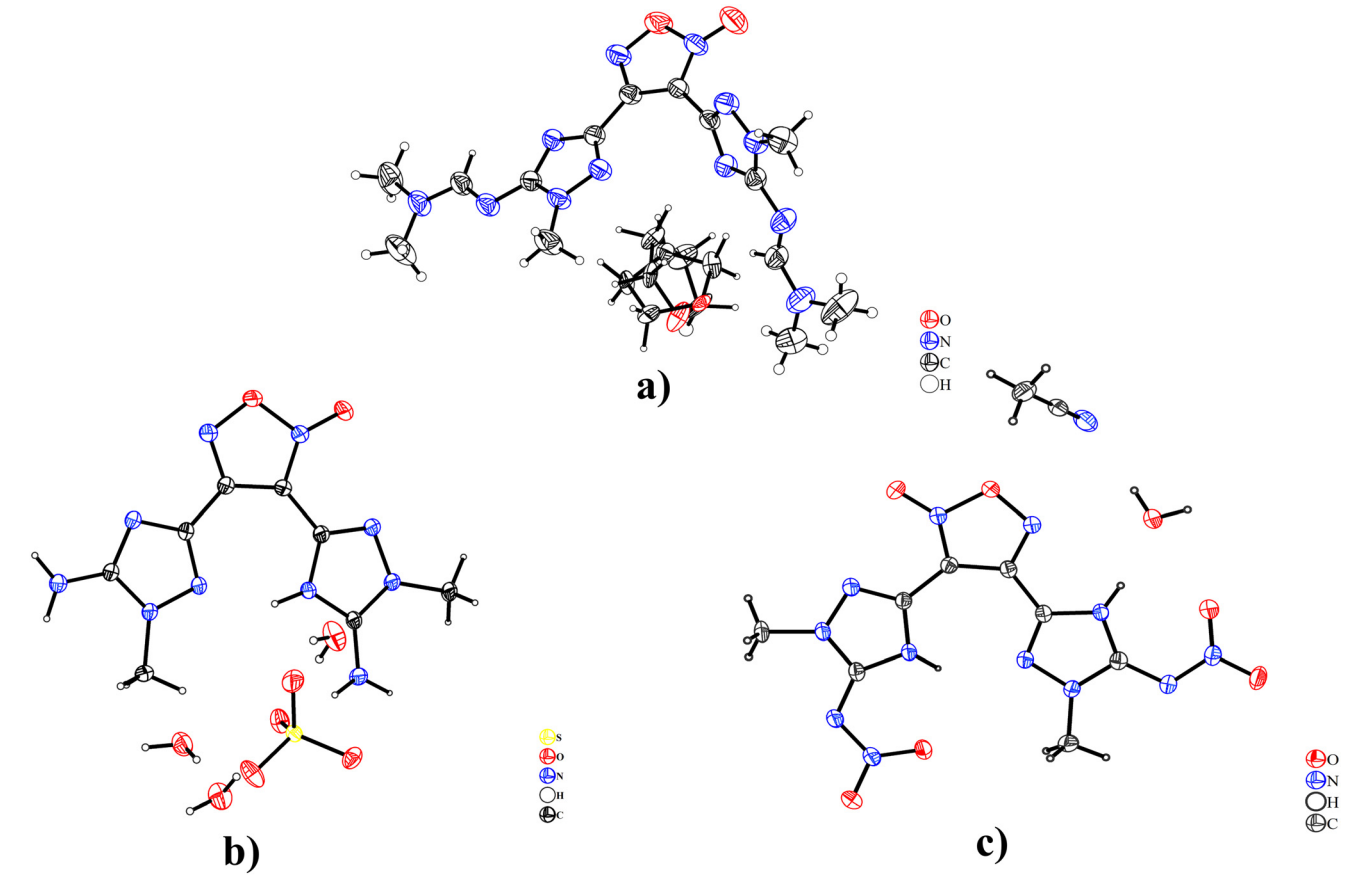


Fig. 5 The single-crystal structure view of compounds **12**, **13**, and **15** corresponds to a), b), and c). Thermal ellipsoids are drawn at 50% probability.

which indicates a significant reduction in heat resistance. This may be due to the instability of the furoxan ring, which could be causing the higher inductive effect of the nitro groups on the triazole ring. Compounds **13** and **15** have better impact sensitivities compared to compound **14**, both exceeding 25 J. This is due to the lower donation heat and the graphene structure of crystal stacking, which can be demonstrated in the next part of the discussion. The crystalline structure of graphene enhances safety by reducing hot spot generation in external impact stimulation through sliding molecular layers (Table 1).

## Structural description

**(1) Structure description of molecules.** The dihedral angle of the compounds was measured using CrystalExplorer software, as shown in Fig. 6. The (b) diagram was created by combining the VMD and the Multiwfn. This was achieved by analysing the interaction region indicator (IRI = 1.1). In the (b) diagram, the covalent bonds between atoms appear in dark blue, steric effects in red, and weak interactions such as hydrogen bonding in light blue and van der Waals interactions in green. It has been observed that compounds **13** and **15** are almost in the same plane, as evidenced by three dihedral angles (−3.95°, 1.7°, −1.13°) and (7.89°, 5.89°, 0.53°, −0.77°, −3.70°) at five dihedral angles respectively in Fig. 6(a). The nitrosamine groups are in one plane with the triazole ring, as evidenced by two dihedral angles (7.89°, −3.70°) in compound **15**. Although compounds **13** and **15** are not strictly fused rings, they are almost in the same plane because of the often neglected weak interactions between intramolecular groups. The triazoles on both sides of compounds **13** and **15** are not symmetrical. The triazole on the furoxan side can be obtained by rotating the other by 180°. This lack of symmetry may be due to the intramolecular interactions between the nitrogen atoms and the methyl and amino groups, constraining all atoms in the same plane in compounds **13** and **15**. This is supported by the IRI analyses in Fig. 6(b).

**(2) Structural description for the cluster of compound 13.** Fig. 7 indicates that several water molecules surrounding the central sulfate molecule spatially combine with the $NH_2$ and $CH_3$ of compound **13** through H-bonding interactions. To describe the stacking of compound **13**, the four oxygen atoms connected to the sulfate molecules of the tetrahedral structure could be grouped into two pairs: (O5[a], O6) and (O5, O6[a]). Additionally, it can be observed that the cluster on either side of the sulfate molecule forms a V-shape, as shown in Fig. 7(b). Fig. 7 shows the H-bonds with cyan dashed lines to understand better how hydrogen bonding interactions result in stacking. Table S2† also provides the hydrogen bonds' group classes and bond lengths. In Fig. 7(a), the oxygen atoms of sulfate can form two groups of hydrogen bonds with the N1 atom of compound **13**: O5···H–N1[b] (1.9605 Å) and O6···H–N1 (1.9435 Å). As a result, the four oxygen atoms of the sulfate molecule can form a cluster conformation with five compound **13** molecules through hydrogen bonding interactions, resulting in a six-molecule cluster. The three water molecules around the sulfate stabilise the crystal stacking. O7 and (O3, O4) are located on both sides of the sulfate molecule in Fig. 7(a). Moreover, O7 can form a hydrogen bond with the H atom of methyl (C1[c]) in (O7···H–C1[c]), and O3 can form a hydrogen bond with the $NH_2$ in (O3···H–N7[d]). In Fig. 7(b), the stacking of compound **13** in layers may be attributed to the hydrogen bonding interactions of the three water molecules within the crystals. Compound **13** in 2D is arranged linearly in a combination of M in the horizontal axis through π···π interactions between molecules, and compound **13** molecules stacked in layers on both sides are connected by sulfate and water molecules, as shown in Fig. S30.† This results in a crystal stacking from 2-dimensional to 3-dimensional. To better observe this stacking structure, the structural diagram of the supramolecule from *a*, *b*, and *c* three-axis directions is given in Fig. S33.†

**(3) Structural description for the cluster of compound 15.** The cluster arrangement of compound **15** can be seen in Fig. 8. Black transparent double arrows are included to more conveniently describe the stacking. Fig. 8(b) shows that the arrows point to the angular alignment axes within the crystal lattice. Fig. 8(a) demonstrates that four compound **15** molecules exhibit centre symmetry on both sides of the double arrows. Compound **15** stacks in the following manner: it rotates around the axis of the black double arrows

**Table 1** The physical and chemical properties of the compounds (**13**–**15**) compared to $H_2BTF$ (ref. 21) and BNTNF (ref. 22)

| Comp. | **13** | **14** | **15** | BNTAF | $H_2BTF$ | LLM-105 |
|---|---|---|---|---|---|---|
| $T_d$[a] [°C] | 278 | 138 | 144 | 139 | 229 | 350 |
| $\rho$[b] [g cm$^{-3}$] | 1.677 | 1.77 | 1.77 | 1.84 | 1.62 | 1.85 |
| N + O[c] [%] | 40 | 56 | 53 | 67 | 67 | 57 |
| $\Delta H_f$[d] [kJ mol$^{-1}$] | 114.83 | 185.45 | 210.95 | 841.5 | −133.76 | −12.95 |
| $D$[e] [km s$^{-1}$] | 6.00 | 8.10 | 8.10 | 8.49 | 7.80 | 8.28 |
| $P$[f] [GPa] | 15.02 | 26.77 | 26.92 | 32.40 | 23.80 | 26.77 |
| $Q_{max}$[g] [kcal g$^{-1}$] | 0.55 | 1.05 | 1.09 | — | — | 1.17 |
| IS[h] [J] | >30 | 15 | >25 | — | <2 | 28.7 |
| OB[i] [%] | −0.63 | −0.26 | −0.23 | −0.05 | −0.216 | −0.216 |

[a] Decomposition temperature (DSC, 5 °C min$^{-1}$). [b] Predicted by ref. 25. [c] Both nitrogen and oxygen. [d] Heat of formation calculated with Gaussian16. [e] Calculated detonation velocities *via* K–J equation. [f] Calculated detonation pressure. [g] Detonation heat. [h] Impact sensitivity. [i] Oxygen balance (OB, %) for $C_aH_bN_cO_d$ OB = 1600 × $(d - a - b/2)/M_w$.

 

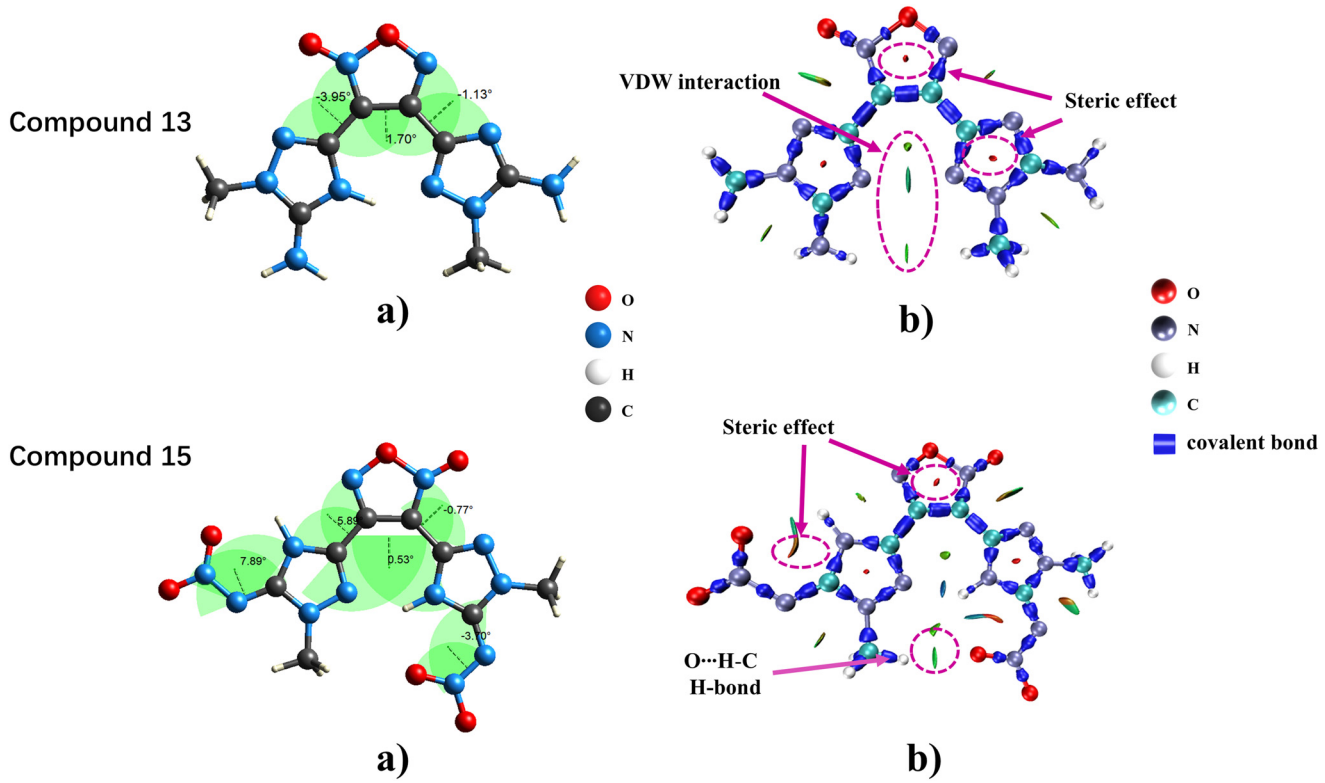


Fig. 6 Molecular structure in crystals (a); IRI analysis (b) of compounds **13** and **15**.

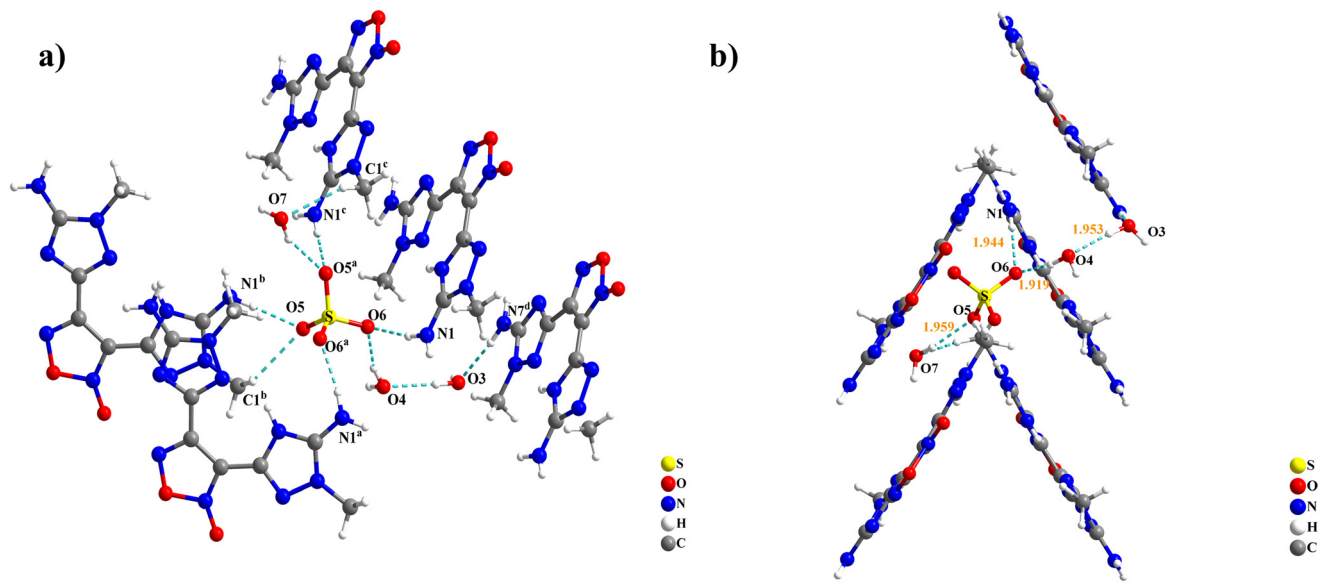


Fig. 7 The cluster structure of compound **13** observed from (a) and (b) two angles.

and spirals in a counterclockwise or clockwise direction, either moving up or down about the double arrows. This rotation and spiral movement completes one entire rotational cycle involving four molecules. Fig. 8(a) clearly illustrates the hydrogen bonding of compound **15** with water and acetonitrile molecules. Specific details about the groups and lengths of the H-bonds depicted are provided in Table S3.† Two hydrogen atoms on the O7 atom form two sets of hydrogen bonds with the O2 atom of compound **15** and the N13 atom of acetonitrile (O2···H–O7, N13···H–O7). The hydrogen on $O7^{b}$ forms a hydrogen bond ($O5^{a}$···H–$O7^{b}$) with $O5^{a}$ located on the other side of compound **15**. The oxygen atom $O4^{a}$ of the furoxan is bonded to the H atom on the methyl group C8 of another compound **15** ($O4^{a}$···H–C8). The

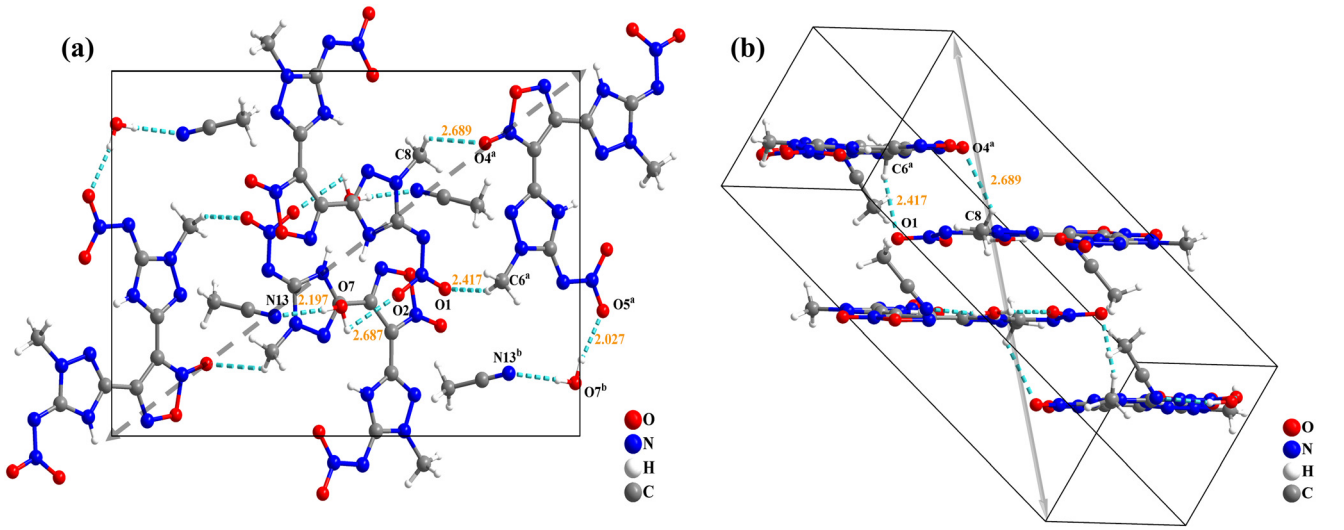


Fig. 8 (a and b) Molecular cluster diagrams of compound **15** observed from two different angles.

H atom on C6[a] is bonded to the O1 atom on the nitro group (O1···H–C6[a]). Fig. 8(b) illustrates how the molecules of compound **15** can form a stacked layer in the crystal space. Compound **15** is arranged horizontally, crossing from left to right. Compound **15** molecules are planar molecules in their spatial structure, unfolding a planar state similar to graphene

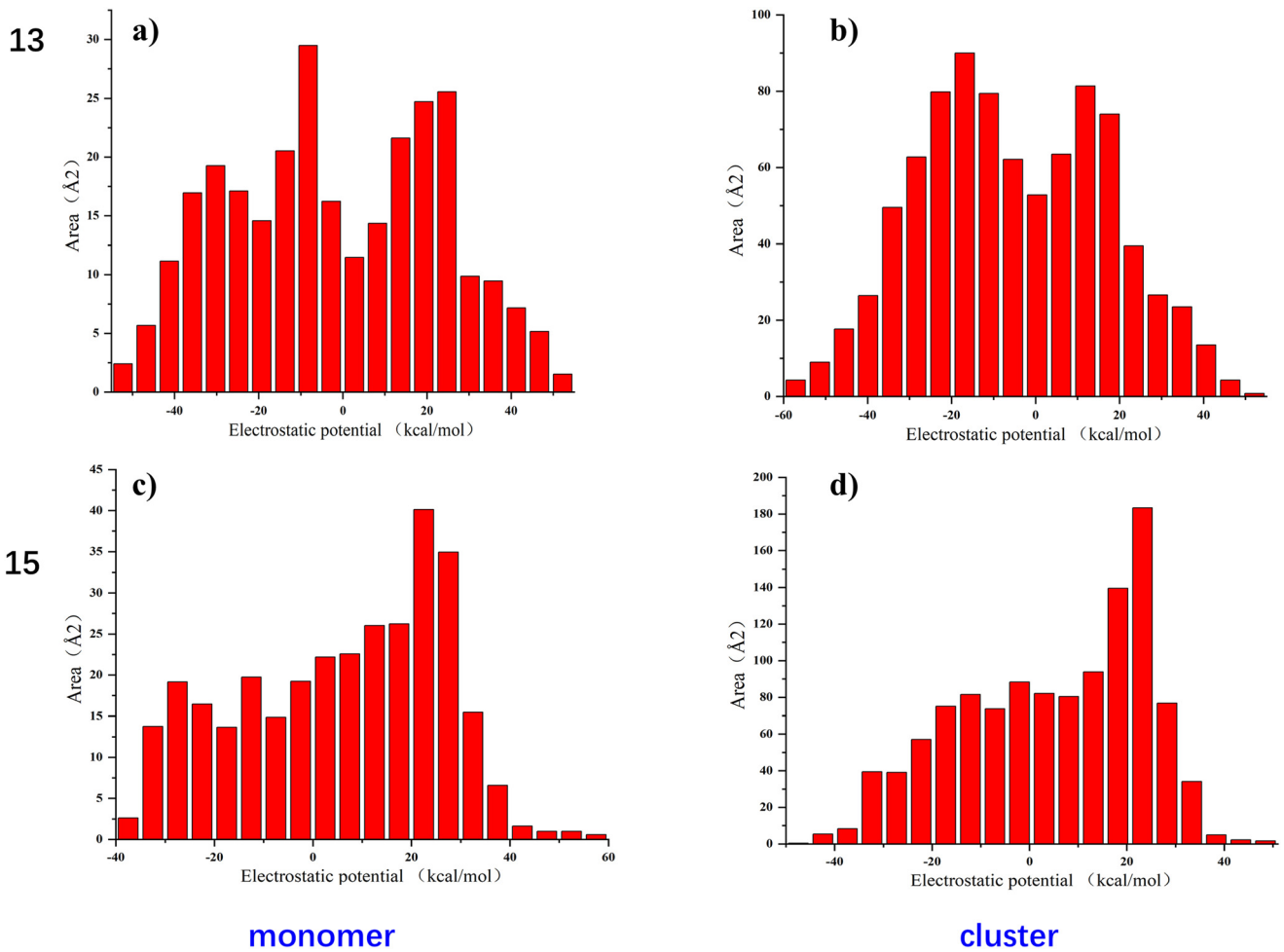


Fig. 9 The electrostatic potential distribution of the monomer (a and c) and clusters (b and d) of compound **13** and compound **15**.

in Fig. S31.† To better observe this stacking structure, the structural diagram of the supramolecule from *a*, *b*, and *c* three axial directions is given in Fig. S34.†

### Wavefunction analysis

**(1) Electrostatic potential distribution analysis.** The research about the electrostatic potential distribution of clusters of energetic compounds usually has more physical significance than that of a monomer. However, the electrostatic potential distribution of clusters has been ignored in previous studies. Compound **13** of the monomer does not show a pattern of positive and negative charges in the overall distribution. Fig. 9(b) shows two humps in the positive potential area (20 kcal $mol^{-1}$) and the negative potential area (−20 kcal $mol^{-1}$) of cluster 13 of electrostatic potential. This indicates that the cluster's electrostatic potential is polarised, which may affect the sensitivity of energetic compounds. When comparing the electrostatic potential of compound **13** in Fig. 9(c and d), it is observed that the positive potential (20 kcal $mol^{-1}$) increases dramatically, which may be caused by the intense negativity of the nitramine group. The polarisation of the cluster is more severe than that of the monomer on compound **15**. The diagrams of the electrostatic potential isosurface of the monomer and clusters are provided in Fig. S28 and S29.† Fig. S29† shows the electrostatic potential isosurface of the penetration effect between individual molecules within each cluster of compounds **13** and **15**, also representing the weak interactions in the cluster. The electrostatic potential of clusters can provide physically meaningful guidance for understanding the effect of sensitivity.

**(2) Hirshfeld surface analysis.** The Hirshfeld surfaces mapped on $d_{norm}$ of compounds **13** and **15** were analysed for colour variations by using CrystalExplorer (the blue colour represents weaker interactions on the surface, while the red colour represents more vital interaction and the white colour represents weaker interactions in general, such as pi–pi stacking, weaker hydrogen bonds, *etc.*) in Fig. 10. The Hirshfeld surfaces are mapped using the shape index and the curvedness provided in Fig. S24.† Decomposed fingerprint plots of compounds **13** and **15** are provided in Fig. S22 and S23.† The area ($d_e > d_i$) represents a hydrogen bond donor on the surface of the molecule on the right-hand side of the fingerprint, and the area with ($d_e < d_i$) represents a hydrogen bond acceptor on the surface of the molecule. The multiple hydrogen atoms of the amino and methyl groups can provide more hydrogen bonding due to compound **13** having two amino groups of methyl on both sides. Additionally, the O atoms of the furoxan and the N atom of the triazole can provide more acceptor sites for H-bonding.

Compound **13** exhibits more red markings than compound **15**, which suggests a higher presence of strong interactions. The O atoms of the nitro group in compound **13** could provide many strong hydrogen bond acceptors. The area of compound **13**'s fingerprints is significantly larger than that of compound **15** in Fig. 10. This confirms that compound **15** has fewer strong interactions. It also can be speculated that compound **13** has

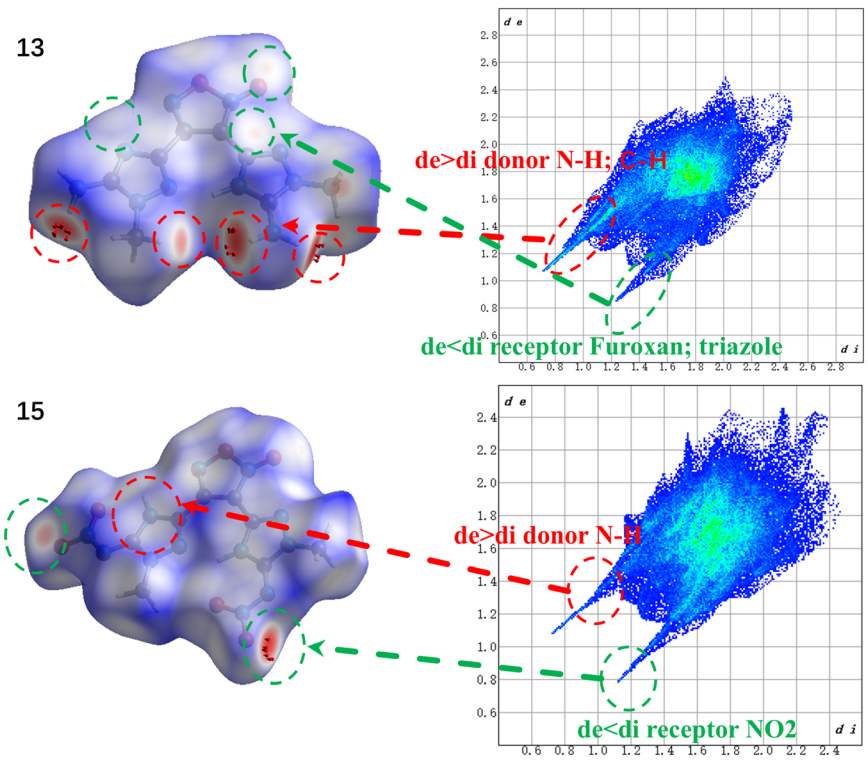


**Fig. 10** The fingerprint of the Hirshfeld surface mapped on $d_{norm}$ of compounds **13** and **15**.

more surface-strong interactions, which could result in a tighter crystal arrangement. In addition, the Hirshfeld surfaces of compounds **13** and **15** exhibit more white and less blue surfaces. The white surfaces suggest that the molecule has relatively weak interactions, such as weak hydrogen bonding and van der Waals interactions. The blue surfaces indicate that the electron density tends to be zero. The less blue surfaces of compounds **13** and **15** suggest that the crystal's pores may be relatively small. This property is significant as it may decrease the impact sensitivity of energetic compounds.

The inside O atoms of compound **13** contribute up to 13.1% on the Hirshfeld surface. The interaction of the inside O atoms with the outside O atoms (O–O) is only 0.4%, making up less than 3% of the total contribution of oxygen atoms. Meanwhile, the inside oxygen of compound **15** can contribute up to 34% due to the oxygen atom of the $NO_2$ group. The interaction of the inside oxygen atom with the outside oxygen atom is only 4.5%, which is less than 15% of the overall contribution of oxygen atoms. In some cases, having fewer interactions between oxygen atoms can increase the safety of energetic compounds. The negative charge of the internal and external oxygen atoms can cause electrostatic repulsion and the formation of hot spots when the molecule in the crystal twists or slips during external simulations—compounds **13** and **15** exhibit lower N–N, C–C, and N–O interaction percentages. The percentages are 7.2%, 2.6%, and 1.2% for N–N, C–C, and N–O interactions in compound **13** and 6.6%, 0.4%, and 4.7% in compound **15**, respectively in Fig. 11. Compound **13** contains more hydrogen atoms due to amino and methyl groups, resulting in increased H–H interactions of 23.2%, compared to compound **15**, which only reaches 13.4%. Compound **13** not only has less O–O, N–N, and other strong mutual solid repulsion but can also form a more robust H-bonding network, which reduces hot spots in the crystal. It can be inferred that compound **13** is a relatively safer energetic compound.

**(3) The enrichment ratio analysis.**[37] The enrichment ratio is a significant calculation derived from analysing interactions between two elements. It indicates the tendency of interaction between two elements in crystal packing. The enrichment ratio can be studied as a function of the surface (%) value. A higher surface (%) for an element suggests increased interaction opportunities on the Hirshfeld surface. Given a specific surface (%), if the enrichment ratio for two elements exceeds 1, it provides strong evidence of heightened interaction. Conversely, a lower value indicates a low tendency of disfavored contacts. The enrichment ratios, surface, and random contacts of the main intermolecular interactions for compounds **13** and **15** are summarised in Table S4.† The crystal structures of both compounds mainly feature H···O type contacts. Compound **13** has well-enriched contacts with $E_{HO}$ = 1.67, while compound **15** has $E_{HO}$ = 1.35. This enrichment is due to the high presence of $S_H$ (49.5%) and $S_O$ (17.1%) in compound **13** and $S_H$ (41.85%) and $S_O$ (29.10%) in compound **15** about the total Hirshfeld surface area. Both compounds also have relatively high $E_{NN}$ = 1.42 and $E_{NN}$ = 1.46 due to the high $S_N$ with an abundance of $S_N$ (21.20%) in compound **13** and $S_N$ (22.50%) in compound **15**, respectively. Additionally, heterocycles of compounds **13** and **15** containing N atoms have a higher propensity to form π···π stacking due to δ+ and δ− polarized atoms, which can form interacting partners contributing to the high $E_{NN}$.

The fundamental structure distinction between compound **13** and compound **15** is the replacement of the hydrogen atoms of the amino groups on both sides with nitro groups. As a result, the $S_O$ (17.1%) of compound **13** is lower than the *So* (29.1%) of compound **15**. Compound **13** also has a lower $E_{CO}$ =

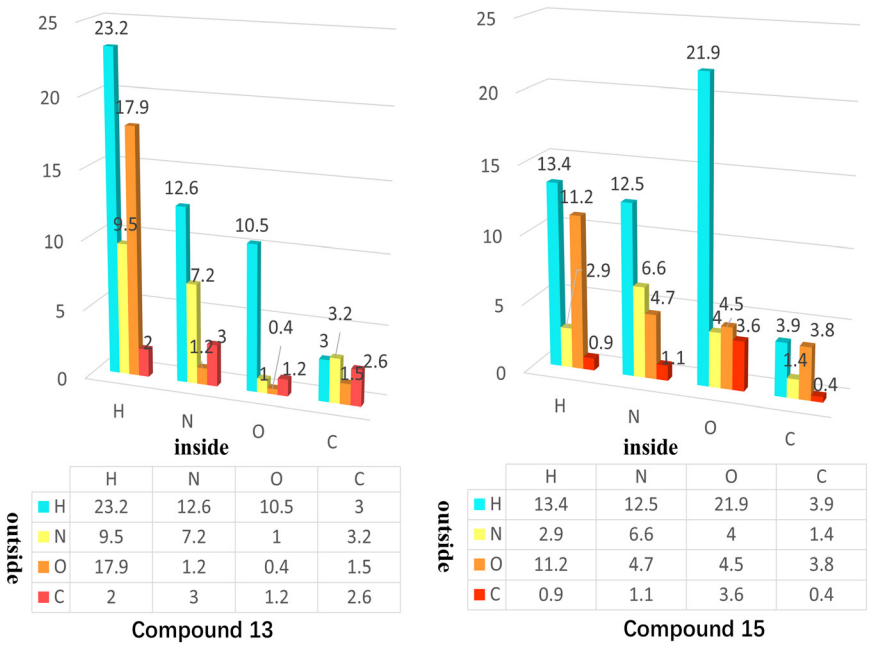


| outside \ inside | H | N | O | C |
|---|---|---|---|---|
| H | 23.2 | 12.6 | 10.5 | 3 |
| N | 9.5 | 7.2 | 1 | 3.2 |
| O | 17.9 | 1.2 | 0.4 | 1.5 |
| C | 2 | 3 | 1.2 | 2.6 |

| outside \ inside | H | N | O | C |
|---|---|---|---|---|
| H | 13.4 | 12.5 | 21.9 | 3.9 |
| N | 2.9 | 6.6 | 4 | 1.4 |
| O | 11.2 | 4.7 | 4.5 | 3.8 |
| C | 0.9 | 1.1 | 3.6 | 0.4 |

**Fig. 11** The interaction statistics between inside and outside atoms of compounds **13** and **15**.

 

0.82 (<1), while compound **15** has an $E_{CO}$ = 1.64 (>1). This indicates that the C···O interaction plays a more significant role in the crystal stacking of compound **15**. In π···π stacking, the oxygen atoms interact with positively charged carbon atoms bonded to heteroatom atoms. Compound **15** has the highest $E_{CC}$ = 2.82, indicating the presence of C···C interactions in the π···π stacking within the heteroaromatic ring across the crystal stacking. This suggests a solid aromatic fused ring in compound **15**. In contrast, compound **13** has an $E_{CC}$ = 0.66 (<1), indicating relatively fewer C–C interactions in the π packing species. The enrichment ratios for H···H, C···H, O···O, and N···O in the two compounds are below 1 (see Table S4†), indicating a lower probability of forming crystal packing. Moreover, the contribution of N···H hydrogen bonding in compound **15** ($E_{NH}$ = 1.03) is higher than that in compound **13** ($E_{NH}$ = 0.99), which suggests that N···H-bond contacts play a more significant role in compound **15**.

**(4) AIM (atoms in molecule) analysis.** Fig. 12 illustrates ten yellow orbs (hydrogen bonding critical points) highlighted in green for compounds **13** and **15** using AIM calculations. By comparing the values of the Laplacian of electron density, the eta index, and $|V_{(BCP)}|/G_{(BCP)}$ of these critical points could examine the nature and strength of hydrogen bonding. Additionally, the yellow path through these vital points represents weak interactions. The bond energies of the hydrogen bonds in the essential points were also calculated using the equation $E_{int} = -223.08 \times \rho(rBCP) + 0.7423$.[38]

A sulfate molecule and three water molecules connect compound **15** through hydrogen bonding, as shown in Fig. 12(a and b). When the Laplacian of electron density ($\nabla^2\rho$) is >0, it can be generally assumed that non-covalent interactions are formed. The $\nabla^2\rho$ values of A–J are all greater than 0 in Table S5.† This indicates that these critical point regions could form hydrogen-bonding interactions. This judgment is based on the $|V_{(BCP)}|/G_{(BCP)}$ criterion for determining the type of bonding. When $|V_{(BCP)}|/G_{(BCP)}$ is <1, interactions in a chemical system are characteristic of closed-shell interactions. When $1 < |V_{(BCP)}|/G_{(BCP)} < 2$, they are intermediate. Three $|V_{(BCP)}|/G_{(BCP)}$ of critical points B (0.8211), I (0.7083), and J (0.6363) are less than 1, while the other seven critical points are >1 and <2. This indicates that the weak interactions of the three critical points (B, I, J) differ from the other seven critical points. When $\eta(r)$ is <1, it indicates non-covalent interactions, with a larger value indicating stronger strength. Comparing the values of $\eta(r)$ and $|V_{(BCP)}|/G_{(BCP)}$ can indicate that the weak interactions of B, I, and J are weaker hydrogen bonds. Judging by the molecular distances between the layers in Fig. 12(a and b), it can be inferred that the weak interactions of the critical points I and J represent weak hydrogen bonding between the

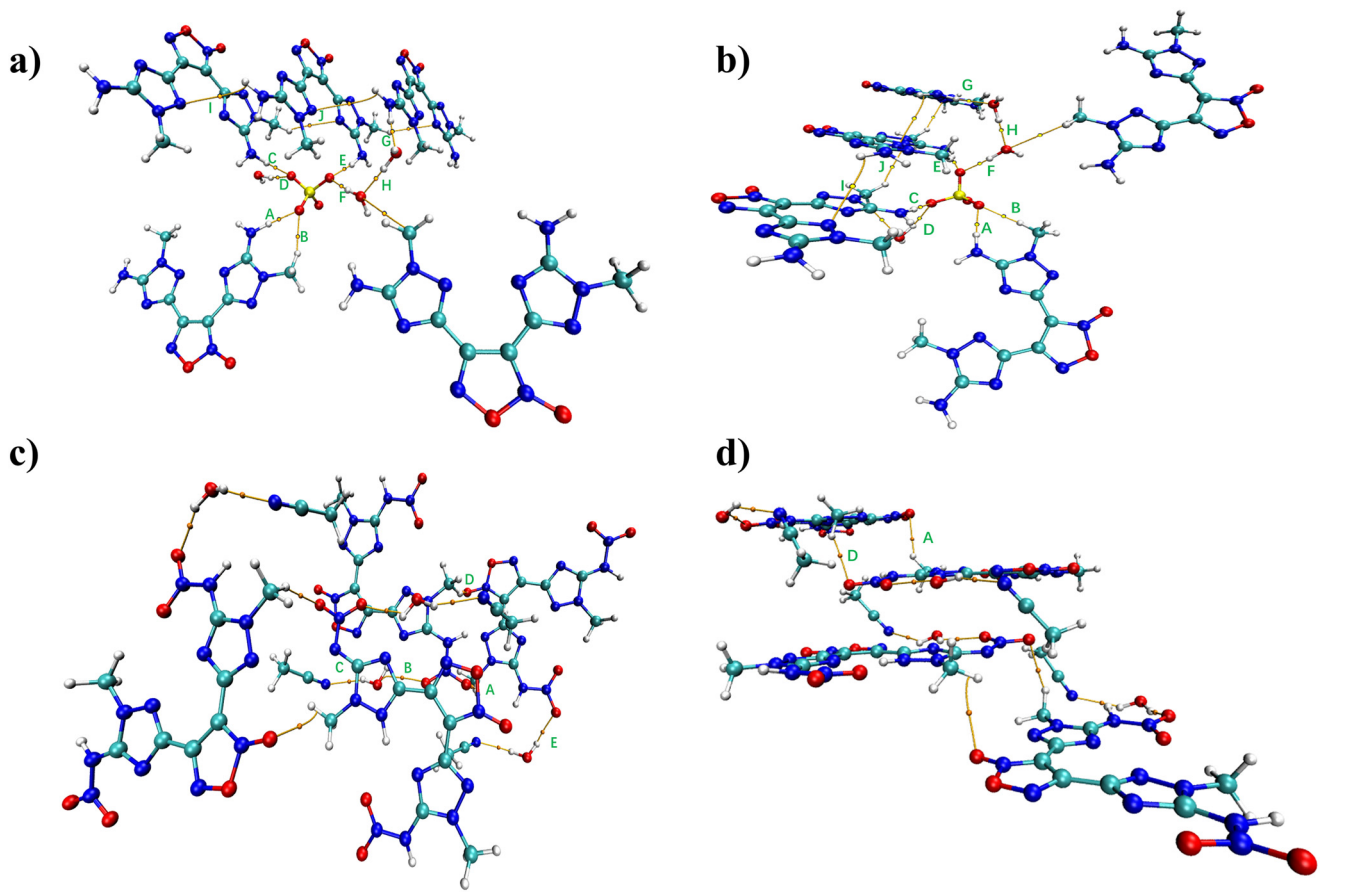


**Fig. 12** Bond critical points in clusters of compound **13** (a and b) and compound **15** (c and d).

molecules of layers. The relatively weak hydrogen bonding at point B is due to the stronger N–H···O interaction of the amino group. The other seven weak interactions are relatively strong. It can be demonstrated that B (2.7170 kcal $mol^{-1}$), I (0.1772 kcal $mol^{-1}$), and J (0.3094 kcal $mol^{-1}$) exhibit lower energies compared to the other critical points, which indicates that these are weak hydrogen bonding points by analysing the strength of hydrogen bonding in terms of electron density and calculating the bond energies ($|E_{int}|$) in Table S5.†

Compound **15** has fewer hydrogen bonds than compound **13**, with only five critical points (A–E) in Fig. 12(c and d). This suggests that the interactions within the cluster molecules of compound **15** are relatively weak by the Laplacian of electron density, the eta index, and $|V_{(BCP)}|/G_{(BCP)}$ of these critical points. The $|E_{int}|$ value indicates that critical points A (1.6479 kcal $mol^{-1}$) and D (1.4043 kcal $mol^{-1}$) represent the hydrogen bonding interactions in compound **15** in Table S5.† In contrast, critical points B and C represent interactions involving a single acetonitrile molecule, a water molecule, and interactions in compound **15**. These interactions are also part of weak hydrogen bonding.

**(5) IGMH and energy framework analysis.** The thin green layer is a π–π stacking layer formed by van der Waals interaction between the layers in Fig. 13(a and b). This demonstrated the presence of hydrogen bonding between layers and van der Waals interactions in the crystal stacking of compounds **13** and **15**. Compound **15** is stabilised by a water molecule that acts as a hydrogen bonding donor and acceptor (within the purple dashed circle) in Fig. 13(b). A hydrogen bond between the water molecule and the N atom on the triazole in the in-plane further enhances the interactions. Hydrogen bonding can effectively tighten the individual molecules per unit volume, increasing the crystal density and reducing the voids in the lattice. The scattered graphs of IGMH are provided in Fig. S27 and S28.† The distribution of dots in the upper left of the scatter graphs indicates that van der Waals interactions and weak hydrogen bonding interactions are spread around compounds **13** and **15**.

## Conclusion

Three novel bis-(1,2,4-triazolyl)-furoxan structures of energetic compounds (**13–15**) were synthesised in this work. However, the experiment demonstrated that compounds **9** and **10** failed to form. The successful synthesis of furoxan may be attributed to the *N*-methylation of active hydrogen on triazole. Although *N*-methylation reduces the energy of bis-(triazole)-furoxan, its

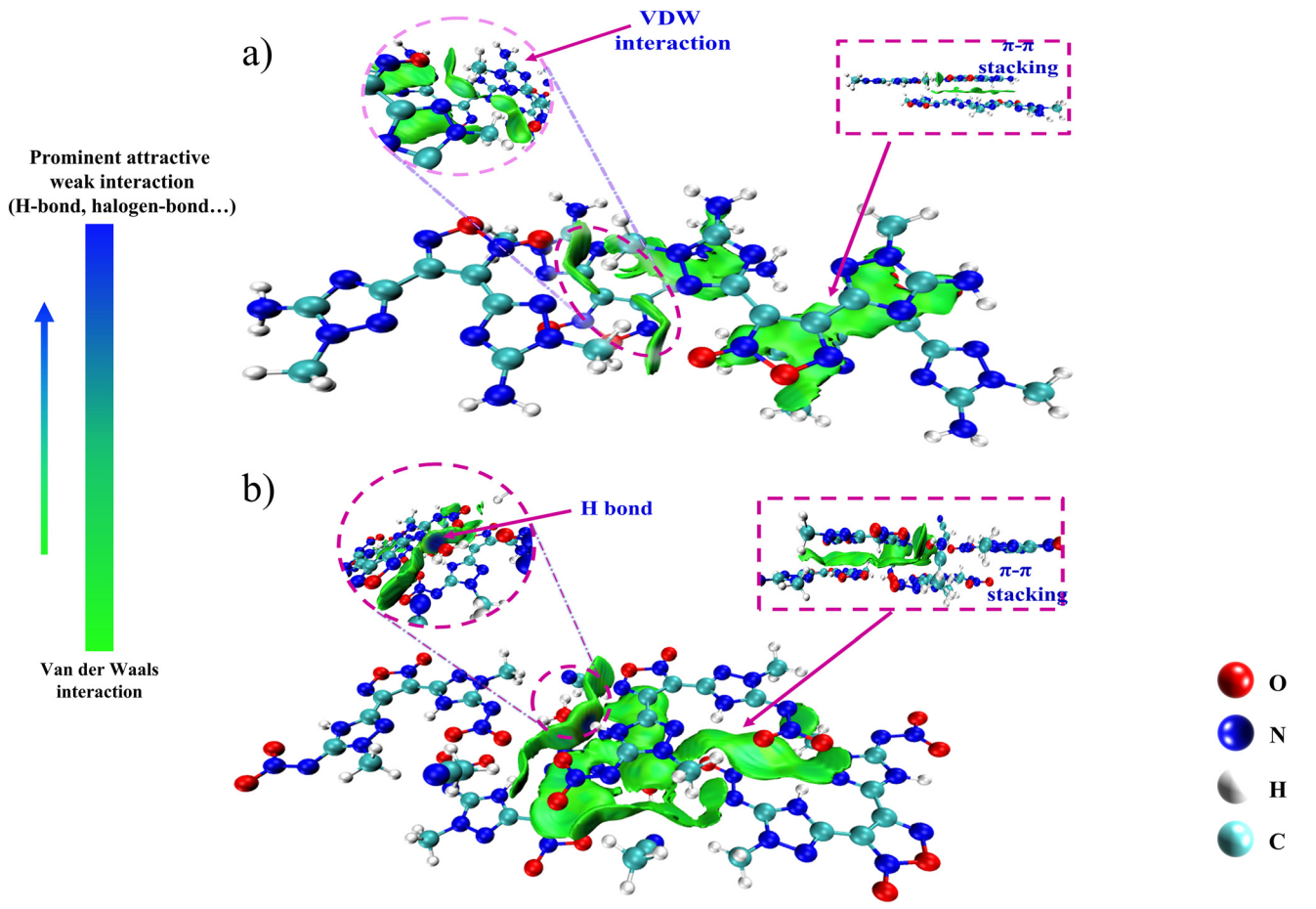


Fig. 13 IGMH analysis of clusters of compound **13** (a) and compound **15** (b).

 

significance can be highlighted in three key ways. Firstly, methylation facilitates the 1,3-dipole reaction, allowing it to proceed smoothly. Secondly, the methyl group acts as an electron-donating group, enabling the amino group to participate effectively in subsequent nitration and oxidation reactions. Finally, methylation introduces a spatial hydrogen-bonding effect in the crystal structure, contributing to the crystals' stacking. The relatively low decomposition temperature of compound **15** (144 °C) may be attributed to the introduction of the nitramine group.

The impact energy of compound **13** (>30 J) is significantly higher than that of the previously reported energetic compound $H_2$BTF (<2 J). Compound **15** has a detonation velocity of 8.10 km $s^{-1}$, lower than that of BNTAF, measured at 8.49 km $s^{-1}$. However, the sensitivity of compound **15** is similar to that of LLM-105, with an estimated sensitivity more significant than 25 J. This indicates that replacing the tetrazolyl group with a 1,2,4-triazolyl group on the furoxan structure maintains the energy level while significantly reducing sensitivity. This also shows that the structure of the bis-triazole-furoxan is crucial for balancing energy output and sensitivity. The excellent sensitivity of compound **15** is partly due to the molecular structure and primarily due to the graphene-like crystal stacking. The structure description of compound **13** and **15** clusters with IRI, IGMH and AMI noncovalent interaction analysis revealed that compound **13** and **15** are planar molecules due to intramolecular interactions. The planar stacking of the molecules is caused by weak hydrogen bonding and intermolecular interactions between the cluster molecules. Analysis of the electrostatic potential distribution shows that by replacing single molecules with clustered molecules to examine the electrostatic potential of molecular surfaces, clustered molecules exhibit a more regular electrostatic potential, which is significant for subsequent studies assessing the sensitivity of energetic compounds.

## Data availability

The data supporting this study's findings are available from the corresponding author upon reasonable request.

## Author contributions

Conceptualisation: Yucun Liu; Jiapeng Wang. Software: Jianhua Wang; Jiapeng Wang. Writing – original draft: Jiapeng Wang; Jianhua Wang. Investigation: Junming Yuan; Yanwu Yu. Supervision: Yankang Zhang. Resources: Xuejian Yan.

## Conflicts of interest

There are no conflicts of interest to declare.

## Acknowledgements

All of the co-authors want to express their gratitude to Professor Yucun Liu for his guidance, academic encouragement, and friendly critique. Jiapeng Wang would also like to thank his family and friends for their support and care throughout his research.

## References

1 G. Romeo, U. Chiacchio, M. H. Keshavarz, H. Motamedoshariati, R. Moghayadnia, M. Ghanbarzadeh and J. Azarniamehraban, *Modern Heterocyclic Chemistry*, 2018, vol. 38, 1047-1252-1102.
2 L. L. Fershtat, M. I. Struchkova, A. S. Goloveshkin, I. S. Bushmarinov and N. N. Makhova, *Heteroat. Chem.*, 2014, **25**, 226–237.
3 L. X. Liang, K. Wang, C. M. Bian, L. M. Ling and Z. M. Zhou, *Chem. – Eur. J.*, 2013, **19**, 14911–14919.
4 E. C. Johnson, E. J. Bukowski, J. J. Sabatini, R. C. Sausa, E. F. C. Byrd, M. A. Garner and D. E. Chavez, *ChemPlusChem*, 2019, **84**, 319–322.
5 E. C. Johnson, J. J. Sabatini, D. E. Chavez, L. A. Wells, J. E. Banning, R. C. Sausa, E. F. C. Byrd and J. A. Orlicki, *ChemPlusChem*, 2020, **85**, 237–239.
6 E. S. Zhilin, D. M. Bystrov, I. V. Ananyev, L. L. Fershtat and N. N. Makhova, *Chem. – Eur. J.*, 2019, **25**, 14284–14289.
7 J. W. Fronabarger, M. D. Williams, W. B. Sanborn, D. A. Parrish and M. Bichay, *Propellants, Explos., Pyrotech.*, 2011, **36**, 459–470.
8 C. Jovené, M. Jacquet, J. Marrot, F. Bourdreux, M. E. Kletsky, O. N. Burov, A.-M. Gonçalves and R. Goumont, *Eur. J. Org. Chem.*, 2014, **2014**, 6451–6466.
9 I. Gospodinov, T. Hermann, T. M. Klapotke and J. Stierstorfer, *Propellants, Explos., Pyrotech.*, 2018, **43**, 355–363.
10 D. Fischer, T. M. Klapötke and J. Stierstorfer, *Eur. J. Inorg. Chem.*, 2014, **2014**, 5808–5811.
11 C. L. He, H. X. Gao, G. H. Imler, D. A. Parrish and J. M. Shreeve, *J. Mater. Chem. A*, 2018, **6**, 9391–9396.
12 L. L. Fershtat and N. N. Makhova, *ChemPlusChem*, 2020, **85**, 13–42.
13 L. L. Fershtat, I. V. Ovchinnikov, M. A. Epishina, A. A. Romanova, D. B. Lempert, N. V. Muravyev and N. N. Makhova, *ChemPlusChem*, 2017, **82**, 1315–1319.
14 E.-C. Koch, *Propellants, Explos., Pyrotech.*, 2016, **41**, 526–538.
15 N. S. Aleksandrova, K. A. Monogarov and A. B. Sheremetev, *Chem. Heterocycl. Compd.*, 2020, **56**, 619–622.
16 J. Ma, H. Yang, J. Tang, G. Zhang, Z. Yi, S. Zhu and G. Cheng, *Dalton Trans.*, 2020, **49**, 4675–4679.
17 A. K. Chinnam, R. J. Staples and J. N. M. Shreeve, *J. Org. Chem.*, 2021, **86**, 7781–7786.
18 L. L. Fershtat, M. A. Epishina, I. V. Ovchinnikov, V. V. Kachala and N. N. Makhova, *Chem. Heterocycl. Compd.*, 2015, **51**, 754–759.
19 A. B. Sheremetev, N. S. Aleksandrova, S. S. Semyakin, K. Y. Suponitsky and D. B. Lempert, *Chem. – Asian J.*, 2019, **14**, 4255–4261.
20 A. A. Larin, A. N. Pivkina, I. V. Ananyev, D. V. Khakimov and L. L. Fershtat, *Front. Chem.*, 2022, **10**, DOI: **10.3389/fchem.2022.1012605**.

21 H. Huang, Z. Zhou, L. Liang, J. Song, K. Wang, D. Cao, C. Bian, W. Sun and M. Xue, *Z. Anorg. Allg. Chem.*, 2012, **638**, 392–400.
22 Y. A. Li, Z. Z. Zhang, Z. X. Ge, B. Z. Wang, W. P. Lai and Y. F. Luo, *Chin. J. Chem.*, 2013, **31**, 520–524.
23 A. A. Dippold, D. Izsák and T. M. Klapötke, *Chem. – Eur. J.*, 2013, **19**, 12042–12051.
24 A. A. Dippold and T. M. Klapötke, *Chem. – Asian J.*, 2013, **8**, 1463–1471.
25 P. Politzer, J. Martinez, J. S. Murray and M. C. Concha, *Mol. Phys.*, 2010, **108**, 1391–1396.
26 L. Kazandjian and J. F. Danel, *Propellants, Explos., Pyrotech.*, 2006, **31**, 20–24.
27 P. R. Spackman, M. J. Turner, J. J. McKinnon, S. K. Wolff, D. J. Grimwood, D. Jayatilaka and M. A. Spackman, *J. Appl. Crystallogr.*, 2021, **54**, 1006–1011.
28 R. F. W. Bader, The Quantum Mechanical Basis of Conceptual Chemistry, *Monatsh. Chem.*, 2005, **136**, 819–854.
29 J. Zhang and T. Lu, *Phys. Chem. Chem. Phys.*, 2021, **23**, 20323–20328.
30 S. Manzetti and T. Lu, *J. Phys. Org. Chem.*, 2013, **26**, 473–483.
31 T. Lu and S. Manzetti, *Struct. Chem.*, 2014, **25**, 1521–1533.
32 T. Lu and Q. Chen, *Chem.:Methods*, 2021, **1**, 231–239.
33 T. Lu and Q. Chen, in *Comprehensive Computational Chemistry*, 2024, pp. 240–264, DOI: **10.1016/b978-0-12-821978-2.00076-3**.
34 T. Lu and F. Chen, *J. Comput. Chem.*, 2011, **33**, 580–592.
35 J. Plumet, *ChemPlusChem*, 2020, **85**, 2252–2271.
36 V. G. Andrianov, *Chem. Heterocycl. Compd.*, 1997, **33**, 1115–1119.
37 C. Jelsch, K. Ejsmont and L. Huder, *IUCrJ*, 2014, **1**, 119–128.
38 S. Emamian, T. Lu, H. Kruse and H. Emamian, *J. Comput. Chem.*, 2019, **40**, 2868–2881.